PNAS RESEARCH ARTICLE | BIOPHYSICS AND COMPUTATIONAL BIOLOGY OPEN ACCESS

Thermodynamic modulation of gephyrin condensation by inhibitory synapse components

Gyehyun Lee[a], Seungjoon Kim[b,c], Da-Eun Hwang[d], Yu-Gon Eom[d], Gyubin Jang[b,c], Hye Yoon Park[e,f], Jeong-Mo Choi[d,1], Jaewon Ko[b,c,1], and Yongdae Shin[a,g,1]

Edited by Tanja Mittag, St. Jude Children's Research Hospital, Memphis, TN; received August 8, 2023; accepted February 5, 2024 by Editorial Board Member Paul Chaikin

Phase separation drives compartmentalization of intracellular contents into various biomolecular condensates. Individual condensate components are thought to differentially contribute to the organization and function of condensates. However, how intermolecular interactions among constituent biomolecules modulate the phase behaviors of multicomponent condensates remains unclear. Here, we used core components of the inhibitory postsynaptic density (iPSD) as a model system to quantitatively probe how the network of intra- and intermolecular interactions defines the composition and cellular distribution of biomolecular condensates. We found that oligomerization-driven phase separation of gephyrin, an iPSD-specific scaffold, is critically modulated by an intrinsically disordered linker region exhibiting minimal homotypic attractions. Other iPSD components, such as neurotransmitter receptors, differentially promote gephyrin condensation through distinct binding modes and affinities. We further demonstrated that the local accumulation of scaffold-binding proteins at the cell membrane promotes the nucleation of gephyrin condensates in neurons. These results suggest that in multicomponent systems, the extent of scaffold condensation can be fine-tuned by scaffold-binding factors, a potential regulatory mechanism for self-organized compartmentalization in cells.

phase separation | biomolecular condensate | synapse | polyphasic linkage

Significance

Macromolecules in cells are compartmentalized into various condensates with composition distinct from the surrounding cellular space. Although condensates consist of multiple species, little is known about how multicomponent phase behaviors of biomolecules are determined. Here, we combine quantitative live-cell imaging, optogenetic manipulation, and atomistic simulations to dissect the thermodynamic phase behaviors of multicomponent systems and their functional implications. Through heterologous expression of inhibitory synapse components, complemented with experiments in neurons, we show that the phase separation of scaffold molecules is modulated by the network of interactions between scaffolds and scaffold-binding proteins. Our findings suggest that biomolecular condensation in living cells can be spatiotemporally regulated through the local availability of scaffold-binding factors.

Biomolecular phase separation has been increasingly recognized as a key organizational principle for various biological processes, including transcriptional and translational regulation, signal transduction, cell polarity, and protein quality control (1, 2). Unlike membrane-bound organelles, membrane-less condensates lack a physical barrier limiting material transports across their boundary, often allowing dynamic molecular exchange with the surroundings. Condensates in living cells are inherently multicomponent systems harboring diverse molecular species, where each component is thought to play different roles in the organization and function of the condensates. For example, scaffolds, often proteins harboring intrinsically disordered regions (IDRs) or tandem interaction domains, display adhesive motifs that drive phase separation and condensate assembly (1, 3–5). In contrast, clients are not major drivers of biomolecular condensation, although they exhibit heterotypic interactions with scaffolds to define condensate composition and function (3, 6).

The thermodynamic basis of the phase separation of single-component systems, such as solutions of purified proteins, has been extensively studied including their phase diagrams and the contributions of different amino acids (7, 8). However, the phase behaviors of multicomponent systems are poorly understood. A recent study demonstrated that heterotypic intermolecular interactions often dominate over the homotypic ones in the phase separation of intracellular condensates (9, 10). Separate coarse-grained simulation studies showed that the phase separation of scaffolds could be differentially modulated depending on the manner in which scaffolds and clients associated with one another (11), a behavior described with the polyphasic linkage formalism (12, 13). In this view, the scaffold architecture can be represented using the stickers-and-spacers framework (14, 15): Stickers are motifs mediating scaffold–scaffold interactions, while spacers are linkers connecting stickers. It has been suggested that features such as the types of client binding sites in scaffolds as well as the valency of clients can strongly influence scaffold phase separation: Binding of monovalent clients to stickers may hinder phase separation, whereas binding of multivalent clients to spacers can promote the thermodynamic stability of scaffold phase separation (11, 16). However, systematic live-cell investigations probing the role of clients in modulating the phase separation of self-associating scaffolds are lacking.

Neuronal synapses, in which various functional condensates with distinct compositions coexist within small subcellular volume, represent an ideal model system for studying multiphase behaviors of multicomponent systems (17, 18). Several previous studies have

The authors declare no competing interest.

This article is a PNAS Direct Submission. T.M. is a guest editor invited by the Editorial Board.

[1]To whom correspondence may be addressed. Email: jmchoi@pusan.ac.kr, jaewonko@dgist.ac.kr, or ydshin@snu.ac.kr.

This article contains supporting information online at https://www.pnas.org/lookup/suppl/doi:10.1073/pnas.2313236121/-/DCSupplemental.

Published March 11, 2024.

shown that many protein complexes involved in synapse organization undergo phase separation (17). For example, a subset of active zone-enriched proteins forms liquid condensates, together with voltage-gated Ca^{2+} channels and synaptic vesicles (19–23). Similarly, highly abundant excitatory postsynaptic density (ePSD) scaffolds, including PSD-95, Shank, Homer, and SynGAP, undergo liquid–liquid phase separation through their network of intermolecular interactions, further concentrating glutamate receptors and membrane proteins in support of excitatory synaptic transmission and plasticity (24–26). Intriguingly, it was recently shown that phase separation also plays a role in the organization of the inhibitory postsynaptic density (iPSD). Purified recombinant gephyrin, an inhibitory synapse-specific scaffold (27), was shown to undergo phase separation, together with the cytoplasmic loops of glycine receptors and $GABA_A$ (γ-amino butyric acid-A) receptors (28, 29). However, how different gephyrin-binding proteins modulate the thermodynamics of gephyrin phase separation and the mechanisms by which the phase behaviors of gephyrin might be exploited for proper assembly and localization of the iPSD in neurons remain to be determined.

Here, we used a subset of iPSD components, including gephyrin, as a model to study the thermodynamic phase behaviors of multicomponent systems. Unlike the ePSD, in which multiple components collectively act together as scaffolds, gephyrin is considered a single major scaffold in the iPSD (30), providing the attractively simple model for the study of multicomponent systems. Using this model, we first characterized the overall phase behaviors of gephyrin in cells as well as the contribution of individual gephyrin domains to condensation. We found that in addition to oligomerization domains, the gephyrin central IDR linker is critical for gephyrin condensation. Linker-swapping experiments and atomistic Monte Carlo (MC) simulations further revealed that the linker-mediated phase separation is not attributable to IDR–IDR interactions, but rather originates from the conformational collapse of the linker as well as electrostatic interdomain interactions. We found that other iPSD components act as clients to differentially modulate the stability of gephyrin condensation, a behavior we analyzed using polyphasic linkage formalism. We also demonstrated that local enrichment of gephyrin-binding proteins can induce the nucleation of gephyrin condensates at the neuronal membrane. Our findings suggest that the formation and spatial distribution of multicomponent condensates can be thermodynamically regulated through a network of intermolecular interactions between condensate components in living cells.

Results

Phase-Separation Behaviors of Gephyrin in Cells. To probe the phase behaviors of gephyrin, we first transiently expressed enhanced green fluorescent protein-tagged gephyrin (EGFP-gephyrin) in human embryonic kidney 293T (HEK293T) cells and monitored its subcellular distribution. We started image acquisition from relatively early time points, approximately 5 h after transfections, to capture concentration-dependent behaviors. When EGFP-gephyrin was expressed at low levels, gephyrin was uniformly distributed throughout the cytoplasm (Fig. 1*A*). As the EGFP-gephyrin expression increased, bright EGFP-gephyrin puncta appeared in the cytoplasm, in line with previous observations (31, 32). Gephyrin puncta formation appeared to occur when gephyrin concentration reached a similar concentration range (*SI Appendix*, Fig. S1), suggesting that gephyrin clustering occurs via phase separation (33). To test this idea, we examined the presence of gephyrin clusters in individual cells over a broad range of expression levels. Consistent with phase separation processes, we found a clear concentration threshold segregating the cell population into two groups: those with and without gephyrin clusters (Fig. 1*B*). When monitored over time, gephyrin clusters gradually grew, frequently reaching up to a few micrometers in diameter, and exhibited occasional fusion events between clusters (Fig. 1*C*), which are typical behaviors of intracellular condensates. After fusion, gephyrin condensates exhibited a rapid relaxation in shape, but they did not fully relax into a round morphology, indicating that gephyrin condensates are not purely in a viscous liquid state. To further characterize the material properties of gephyrin condensates, we next analyzed the diffusive mobility of gephyrin using fluorescence recovery after photobleaching (FRAP) assays. Intriguingly, we found a time-dependent change in the internal mobility of gephyrin, with clusters at ~5 h after transfection exhibiting ~40% of fluorescence recovery and those at ~18 h showing much reduced recovery (Fig. 1*D*). This increase in the immobile fraction of gephyrin condensates suggests that after initial phase separation, individual gephyrin molecules within clusters undergo time-dependent rearrangements that likely involve a change in the network of intermolecular interactions toward tighter bindings and less liquidity (34, 35).

To further probe the internal rearrangement process in gephyrin condensates, we monitored temporal changes in gephyrin concentration within condensates during their growth. Interestingly, we found that the fluorescence intensities of gephyrin condensates gradually increased over time until reaching a plateau (Fig. 1 *E* and *F*). Since the fluorescence intensity of small subcellular structures can be underestimated owing to diffraction limits, we examined the effect of condensate size on brightness. As a control, we imaged light-inducible FUS_N-Corelet condensates (36), which behave as a binary phase-separating system, where the ferritin core particles of IDR oligomers undergo phase separation into two coexisting phases with well-defined component concentrations (36). We found that under our imaging conditions, the dense-phase concentration of the Corelet system can be reliably quantified when the radius of condensates was larger than ~0.75 μm (Fig. 1 *E* and *G*). In contrast, gephyrin condensates exhibited a fluorescence increase even above this size limit (Fig. 1 *F* and *G*), indicating that the observed increase in gephyrin concentration during condensate growth is not an artifact of diffraction-limited imaging, but instead is an intrinsic property of gephyrin condensates. These results, together with the FRAP data, suggest that the initial molecular configuration immediately after gephyrin phase separation might represent a state corresponding to the local thermodynamic minimum of the system and that the system slowly relaxes into a lower energy state with higher packing densities.

The Role of the Disordered C Domain in Gephyrin Phase Separation. Gephyrin consists of two globular domains, G and E, and a central linker region, termed the C domain (27, 37, 38). The G and E domains are known to undergo homotrimerization and homodimerization, respectively (39, 40) (Fig. 2*A*). Previous studies showed that homo-oligomerization of G and E domains is required for gephyrin clustering (39, 41). Thus, in context of the stickers-and-spacers framework (14), the G and E domains harbor stickers that drive associative interactions between gephyrin scaffolds, whereas the disordered C domain appears to act as a spacer that connects stickers. To probe the role of the C domain in gephyrin phase separation, we generated a gephyrin-deletion construct lacking the C domain, termed G-E, and examined its clustering behavior in HEK293T cells. Unexpectedly, we found that deletion of the C domain completely abolished gephyrin phase separation (Fig. 2*B*). Similarly, replacing the C domain with a short linker (four repeats of GGS tripeptide) strongly hindered gephyrin clustering (*SI Appendix*, Fig. S2*A*).

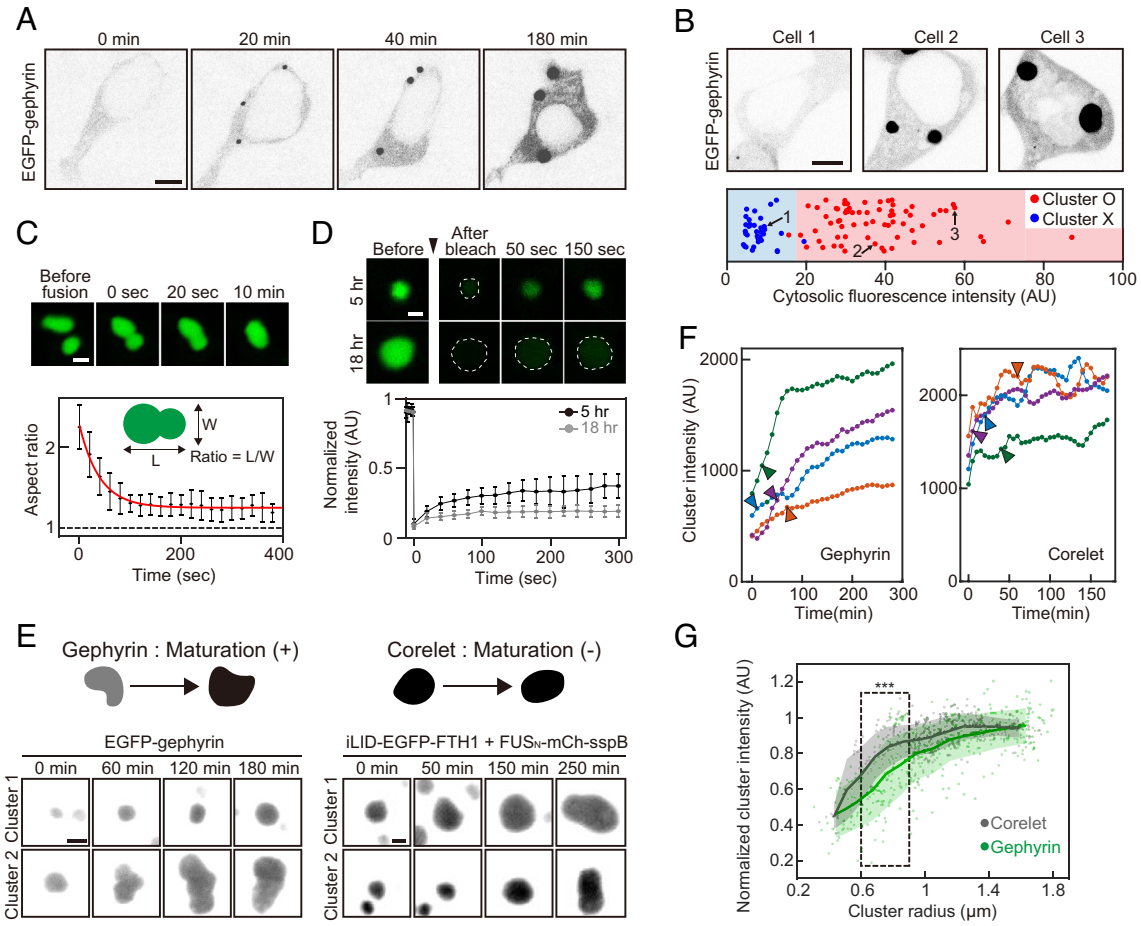

Fig. 1. The concentration-dependent phase separation of gephyrin. (*A*) Inverted black and white time-lapse images of EGFP-tagged gephyrin in the HEK293T cell. The cell was transfected with EGFP-gephyrin around 5 h prior to imaging. (Scale bar, 6 μm.) (*B*) (*Top*) Fluorescence images of EGFP-tagged gephyrin in HEK293T cells. (Scale bar, 6 μm.) (*Bottom*) Cytosolic fluorescence intensity of individual EGFP-gephyrin expressing cells. Data points are color-coded for the presence of condensates. n = 3 experiments (total 105 cells). Data points are randomly scattered along the vertical axis for better readability. (*C*) (*Top*) Fluorescence time-lapse images of two gephyrin clusters undergoing fusion. (Scale bar, 2 μm.) (*Bottom*) Mean aspect ratios of the fused clusters as a function of time. A red curve denotes an exponential fit to data. Error bars ± SD; n = 8 (from five cells). (*D*) (*Top*) FRAP images of gephyrin clusters at the indicated time points after transfection. Cluster boundaries are indicated with dashed lines. (Scale bar, 1 μm.) (*Bottom*) FRAP recovery curves of gephyrin clusters at the indicated time points after transfection. Error bars ± SD; n = 5 (from five cells) for each condition. (*E*) Fluorescence images of gephyrin and FUS Corelet clusters over time. Schematic for the maturation of condensates that accompanies an increase in component concentration is shown. Scale bar, 2 μm (gephyrin); 1 μm (Corelet). (*F*) Examples of fluorescence intensity changes within gephyrin (*Left*) and Corelet (*Right*) cluster over time. Data points are moving-averaged over every three values. Time points at which condensate radius first exceeds 0.75 μm are indicated as arrowheads. (*G*) Fluorescence intensities of individual gephyrin and Corelet clusters, normalized based on maximum values within individual cells, are plotted against cluster radius. Clusters at several time points were measured from multiple cells for each sample type. Solid lines and shaded areas indicate the average and SD of data points located within a 0.3-μm window. Data points located within 0.6 to 0.9 μm interval are compared using Welch's *t* test, ***$P < 0.0001$. Corelet, n = 325 (12 cells); gephyrin, n = 410 (16 cells).

These observations prompted us to investigate the mechanism by which the C domain of gephyrin facilitates phase separation. Many of the proteins with IDRs are known to undergo phase separation through homotypic associations (4, 35, 42). We thus sought to probe the self-association capacity of the C domain using a well-established optoDroplet system (33). The optoDroplet system, comprising a fusion protein and mCherry-tagged Arabidopsis cryptochrome 2 (mCh-Cry2), enables the control of intracellular phase separation using external light input and has been widely used to study the phase-separation capacity of several protein domains (9, 33). Notably, the saturation concentration of the specific optoDroplet construct is a strong indicator of the strength of the homotypic interaction exhibited by the fusion protein domain (33, 43) (*SI Appendix*, Fig. S2*B*). We used the gephyrin C domain as an IDR fusion to the optoDroplet and probed its light-dependent phase-separation behaviors. Surprisingly, we found that the optoDroplet with the gephyrin C-domain fusion exhibited little clustering, a behavior drastically different from that of self-associating FUS or DDX4 IDR fusions (Fig. 2*C*). These results suggest that the requirement of the C domain for gephyrin phase separation reflects the operations of mechanisms that do not involve IDR–IDR self-association.

To better understand the role of the central IDR linker in gephyrin condensation, we investigated whether other types of IDRs could substitute for the gephyrin C domain in driving phase separation. To this end, we employed IDRs from FUS (residues 5 to 164), DDX4 (residues 2 to 161), and G3BP1 (residues 143 to 334), which have all been extensively characterized with respect to their phase-separation behaviors (4, 8, 44) (*SI Appendix*, Fig. S2 *C–F*). Notably, unlike FUS and DDX4 IDRs, G3BP1 IDR is known to be dispensable for phase separation (44). The gephyrin variants G-FUS_{IDR}-E, G-$DDX4_{IDR}$-E, and G-$G3BP1_{IDR}$-E, in which the C domain was replaced with the corresponding IDR, were expressed and their phase-separation behaviors were examined (Fig. 2*D*). Interestingly, these variants exhibited drastically different clustering tendencies, with G-$DDX4_{IDR}$-E and G-$G3BP1_{IDR}$-E showing a phase-separation capacity as strong as that of WT gephyrin and G-FUS_{IDR}-E remaining diffusely distributed in most cells (Fig. 2*D*).

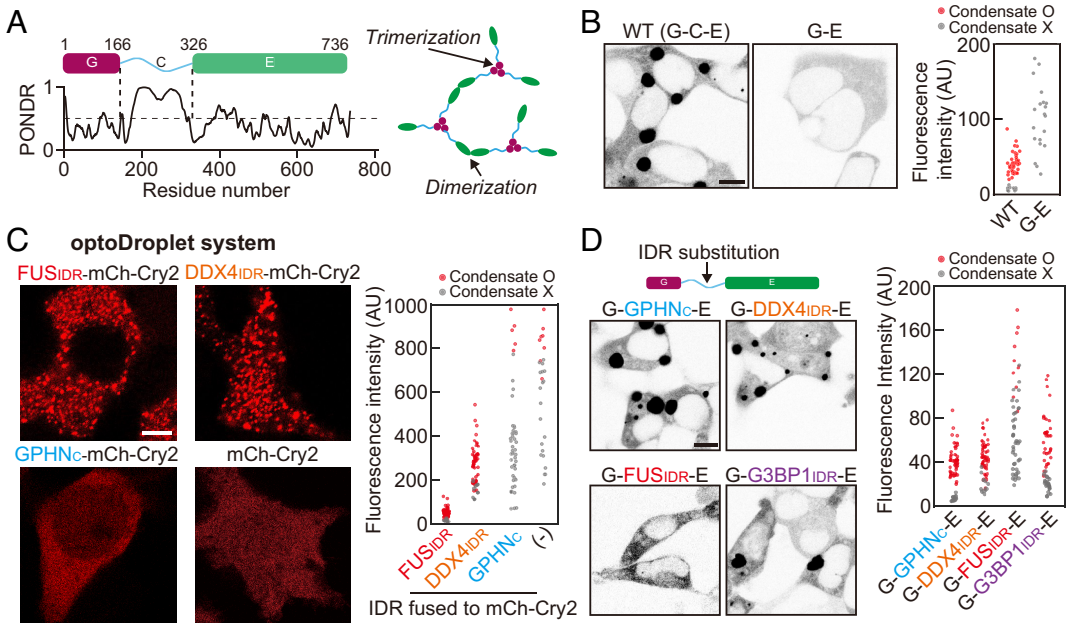

Fig. 2. The role of the C domain in gephyrin phase separation. (*A*) (*Left*) Schematic of the domain organization of gephyrin. PONDR, prediction of intrinsic disorder. (*Right*) Gephyrin G and E domains undergo homotrimerization and dimerization, respectively. (*B*) (*Left*) Fluorescence images of EGFP-tagged gephyrin WT and gephyrin G-E in HEK293T cells. (Scale bar, 8 μm.) (*Right*) Cytosolic fluorescence intensities of HEK293T cells expressing gephyrin WT or G-E. (*C*) (*Left*) Fluorescence images of various optoDroplet constructs in HEK293T cells after activation of identical blue-light conditions. (Scale bar, 6 μm.) (*Right*) Cytosolic fluorescence intensities of HEK293T cells expressing different optoDroplet constructs. (*D*) (*Left*) Fluorescence images of EGFP-tagged gephyrin variants with different IDR substitutions. (Scale bar, 8 μm.) (*Right*) Cytosolic fluorescence intensities of HEK293T cells expressing gephyrin variants with different IDR substitution.

These results underscore the fact that the presence of oligomerization domains such as G and E is not sufficient for gephyrin phase separation and that the central IDR linker serves important roles beyond simply connecting G and E domains. Moreover, our findings further confirm that the capacity of the central linker for homotypic associations is not required for gephyrin phase separation. Notably, gephyrin variants with different IDR linkers, including even the poorly phase-separating FUS IDR replacement, exhibit similar maturation behaviors (*SI Appendix*, Fig. S3), suggestive of a distinct maturation mechanism from condensation.

A comparison of the sequences of different IDRs tested here revealed a correlation between the fraction of charged residues in the IDR and its phase separation capacity in the context of gephyrin substitution (*SI Appendix*, Fig. S2 *C–G*). Specifically, FUS IDR is composed mostly of uncharged and polar residues, whereas the other IDRs that support robust phase separation of gephyrin harbor a high fraction of charged residues (*SI Appendix*, Fig. S2 *G* and *H*). Thus, the central IDR of gephyrin critically contributes to phase separation of the full-length protein via a mechanism likely involving charged residues, yet independent of homotypic associations of the IDR.

The Network of Electrostatic Interactions Around the Gephyrin C Domain. We then sought to probe the relative contribution of different segments along the C domain to the phase separation of gephyrin. To this end, we divided the gephyrin C domain into four subregions (C_1 to C_4) of equal length (40 amino acids each) and generated a series of gephyrin variants in which the C domain was replaced with the individual subregions (termed "G-C_i-E") (Fig. 3*A*). Notably, each subregion differed in terms of its charge distribution such that C_1 and C_2 contained abundant negatively charged residues, C_3 was slightly positively charged, and C_4 contained significantly more positively charged residues. Interestingly, we found that each gephyrin variant exhibited markedly different phase-separation behaviors, with the G-C_4-E variant showing phase separation capacity as strong as that of WT gephyrin (Fig. 3*B*). In contrast, clustering was significantly reduced in the G-C_3-E variant, and phase separation was completely abolished in both G-C_1-E and G-C_2-E variants (Fig. 3*B*). Consistent with the critical role of the C_4 subregion, deletion of the C_4 subregion (ΔC_4) from full-length gephyrin caused approximately a fourfold increase in saturation concentration compared with WT (Fig. 3*B*).

To study the roles of positively charged residues in the C_4 subregion in phase separation, we generated full-length gephyrin variants in which four or all eight positively charged residues in the C_4 subregion were mutated to negatively charged ones, termed KR/DE4 and KR/DE8, respectively, and examined their phase-separation behaviors (Fig. 3*C* and *SI Appendix*, Fig. S4*A*). We found that as the number of positively charged residues decreased, the saturation concentrations progressively increased (Fig. 3*C*). To further validate the importance of positively charged residues, we tested whether adding positively charged residues rescued the otherwise poor phase-separation behavior observed in the G-FUS_{IDR}-E variant (Fig. 2*D*). To this end, we replaced a total of eight amino acids (four glycine and four serine residues) near the C-terminal end of FUS_{IDR} with positively charged lysine or arginine residues (*SI Appendix*, Fig. S4*B*). Strikingly, the G-FUS_{IDR}(GS/KR8)-E construct showed robust phase-separation capacity comparable to that of WT gephyrin (Fig. 3*D*). Thus, our findings indicate that positively charged residues positioned near the C-terminal end of the C domain are key determinants driving gephyrin phase separation.

To further understand the molecular mechanism through which positively charged residues in the C domain contribute to phase separation, we next performed atomistic MC simulations with the ABSINTH implicit solvation model (45, 46). In this simulation, we considered the dimerized form of two E domains, with one linked to the C domain, allowing us to probe intradomain interactions within the C domain as well as interdomain ones between the C and E domains (Movies S1, S2, and S3). We removed the G domain in simulation to reduce the computational cost of IDR conformational sampling and froze the geometry of the dimerized

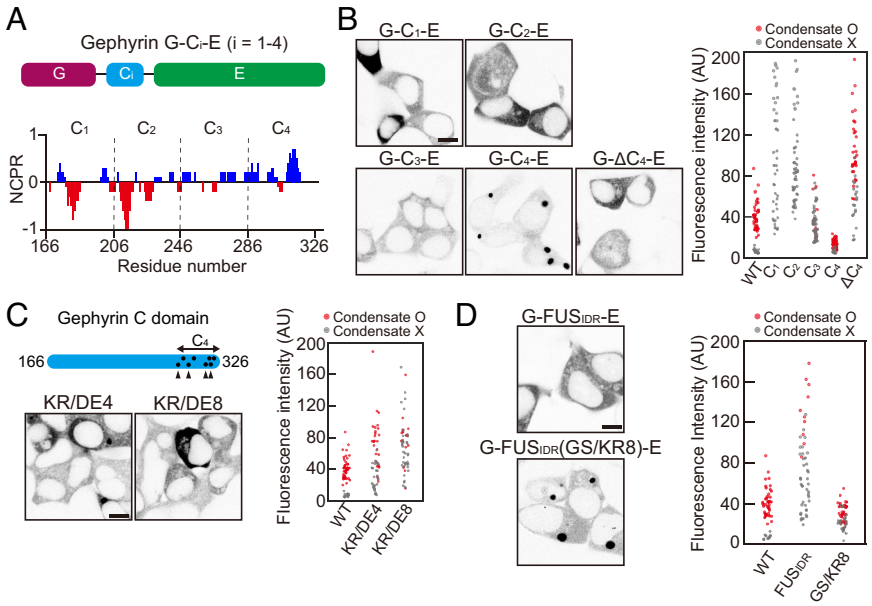

Fig. 3. The positive charges near the C-terminal end of the C domain are important for phase separation. (*A*) Schematic of gephyrin variants with C-domain truncation. Net charge per residue plot of the gephyrin C domain, calculated with a sliding window of 5 residues. (*B*) (*Left*) Fluorescence images of EGFP-tagged gephyrin variants with different C-domain truncation or C_4 deletion in HEK293T cells. (Scale bar, 8 μm.) (*Right*) Cytosolic fluorescence intensity of HEK293T cells expressing gephyrin WT or variants with different C-domain truncations or C_4 deletion. (*C*) (*Top Left*) Schematic of gephyrin variants with positively charged residues mutated into negatively charged ones (KR/DE4 and KR/DE8). Dots indicate positively charged residues in the C_4 subregion mutated in KR/DE8, and arrowheads denote the locations of mutated residues in both KR/DE4 and KR/DE8. (*Bottom Left*) Fluorescence images of gephyrin variants, KR/DE4 and KR/DE8 in HEK293T cells. (Scale bar, 8 μm.) (*Right*) Cytosolic fluorescence intensity of HEK293T cells expressing gephyrin WT or variants. (*D*) (*Left*) Fluorescence images of EGFP-tagged G-FUS_{IDR}-E and G-FUS_{IDR}(GS/KR8)-E in HEK293T cells. (Scale bar, 8 μm.) (*Right*) Cytosolic fluorescence intensity of HEK293T cells expressing gephyrin WT or variants.

E domains (Fig. 4*A*). We first compared thermal fluctuations of WT, KR/DE4, and KR/DE8 variants of the gephyrin C domain (Fig. 4*B*). Interestingly, we found that, as the number of positively charged residues near the C-terminal end increased, the C domain adopted more collapsed configurations (Fig. 4 *B* and *C*). This behavior also manifested as more well-defined subpopulations in the structural ensemble of WT gephyrin than in those of mutant systems (*SI Appendix*, Fig. S5 *A* and *B*). Similar behaviors were observed in the simulation of the C-domain variants in isolation (*SI Appendix*, Fig. S5 *C* and *D*).

To map the specific residues that mediate intra- and interchain interactions, we then computed pairwise contact frequencies between individual residues in the C and E domains (*SI Appendix*, Fig. S5 *E* and *F*). A comparison of the contact frequencies of the WT with those of the charge mutant, KR/DE8, revealed several hotspots of intra- and interchain interactions (Fig. 4 *D* and *E* and *SI Appendix*, Fig. S5*G*). Overall, we found that the removal of positively charged residues in the C_4 subregion led to a decrease in interdomain interactions; residues involved in interdomain interactions were clustered at the C-terminal half of the C domain (i.e., C_3 and C_4 subregions); and hotspots of intrachain interactions involved residues 580 to 610 of the E domain (region 1, Fig. 4 *D* and *E*). Interestingly, this latter region corresponds to vertebrate-specific loops containing several aspartic acids that were previously reported to be important for gephyrin clustering (47). Our simulation predicts that multiple contacts between the C_4 subregion and these loops are lost when the positively charged residues in C_4 are replaced with negatively charged ones. It also predicts that interactions between the C domain and residues 420 to 440 of the neighboring E domain are largely lost in the KR/DE8 variant (region 2, Fig. 4 *D*–*F*). Notably, the corresponding subregion of the E domain is spatially proximal to the C domain of the neighboring chain and largely negatively charged (Fig. 4*F*). Consistent with our simulation results, a gephyrin variant, with its six negatively charged residues in this subregion of E domain replaced with positively charged ones, showed impaired clustering behaviors (*SI Appendix*, Fig. S5*H*). Because the intrachain transient interactions that cause single-chain collapse can be utilized to create interchain transient interactions that lead to phase separation (48), we conclude that the positively charged residues near the C-terminal end of the C domain act as a hub for mediating a network of intra- and interchain interactions.

The Gephyrin C Domain Is Essential for GABAergic Synaptic Targeting and Function in Cultured Hippocampal Neurons. We next examined whether deletion of the gephyrin C domain also affects gephyrin-mediated GABAergic synaptic targeting in hippocampal cultured neurons. To this end, we transfected cultured hippocampal neurons at 10 days in vitro (DIV10) with EGFP-tagged gephyrin or the G-E variant and immunostained the transfected neurons using antibodies against VGAT (vesicular GABA transporter) and the postsynaptic $GABA_A$ receptor γ2 subunit ($GABA_AR\gamma2$) at DIV14. This analysis showed that gephyrin WT was primarily localized to GABAergic synaptic sites, whereas the gephyrin G-E variant was diffusely distributed along the dendrites of transfected neurons (Fig. 5 *A*–*D*). Moreover, overexpression of gephyrin WT, but not gephyrin G-E, significantly increased $VGAT^+GABA_AR\gamma2^+$ puncta density without changing puncta size. These results suggest that the gephyrin C domain is critical for the GABAergic synapse-promoting effects of gephyrin. To corroborate the anatomical results, we performed whole-cell patch-clamp recordings of cultured hippocampal neurons expressing gephyrin WT or G-E. The frequency, but not the amplitude, of miniature inhibitory postsynaptic currents (mIPSCs) was significantly reduced in neurons expressing gephyrin G-E, compared with those expressing control (EGFP alone) or gephyrin WT (Fig. 5 *E*–*G*). Collectively, these data suggest that the gephyrin C domain is critical for the gephyrin-mediated GABAergic synapse organization in cultured hippocampal neurons.

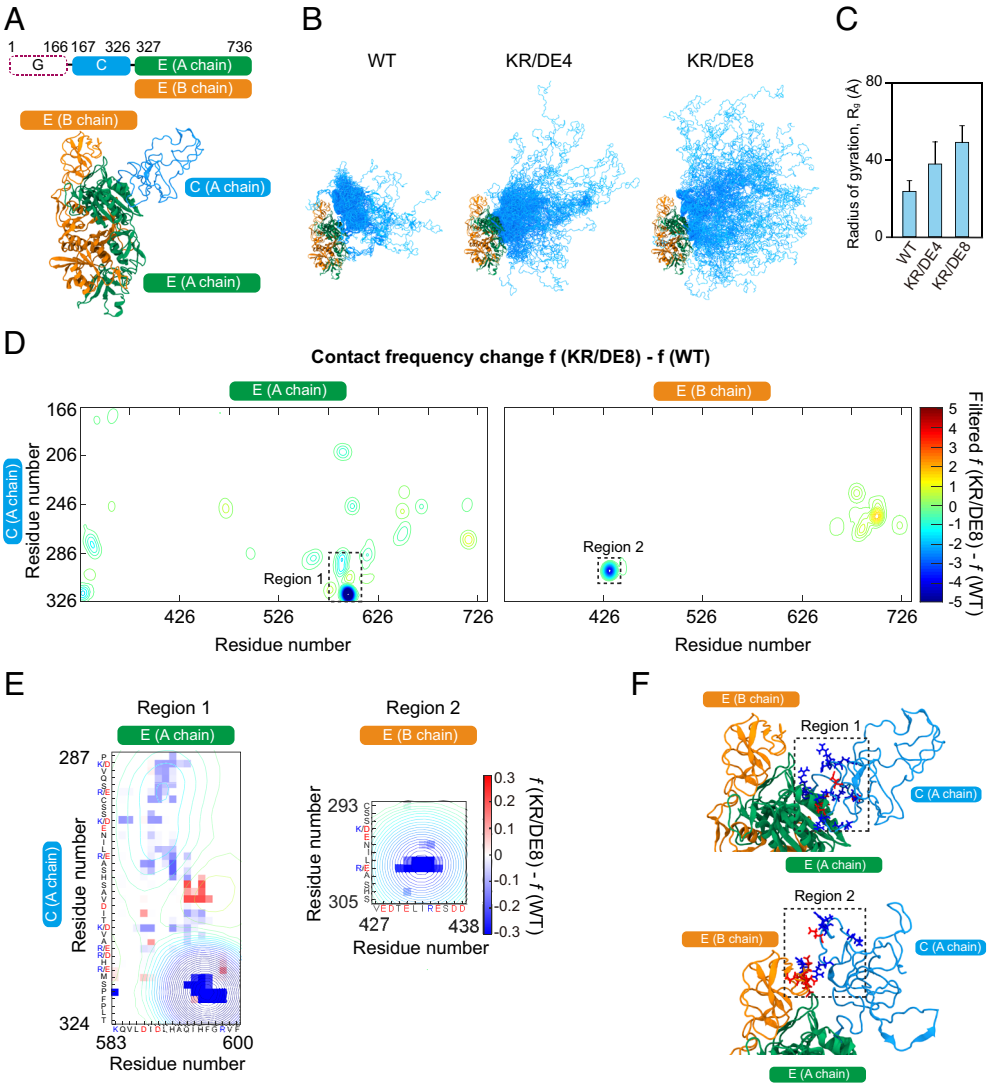

Fig. 4. Atomistic simulations reveal the details of intra- and interdomain interactions of gephyrin. (*A*) Domain architecture and 3D structure of the model system used in simulations. Different colors indicate different domains, as noted in the domain architecture. (*B*) Structural ensembles of gephyrin WT and different variants. Domains are color-coded same as panel (*A*). (*C*) Radii of gyration for the C domain. Error bars ± SD; WT, 23.6 ± 5.5 Å; KR/DE4, 37.9 ± 11.5 Å; KR/DE8, 49.1 ± 8.7 Å. (*D*) Contact frequency difference between gephyrin WT and KR/DE8. For each construct, residue-by-residue pairwise contact frequency maps were first generated (*SI Appendix*, Fig. S5 *E* and *F*), and then, the frequency differences (*SI Appendix*, Fig. S5*G*) were filtered with Gaussian function for readability (*Materials and Methods*). Two regions that show significant reduction in contact frequency are highlighted by dashed boxes. (*E*) Enlarged map of regions 1 and 2 in (*D*). Pixelated images of raw contact frequency difference are overlaid on the contours of filtered data in (*D*). (*F*) Simulation snapshots showing detailed interactions corresponding to regions 1 and 2. Negatively and positively charged residues in the indicated regions are colored in red and blue, respectively.

To corroborate the role of the positive charges in the gephyrin C domain in regulating inhibitory synapses, we also examined whether the ΔC_4 variant of gephyrin, which lacks the positively charged region of the C domain, acts similarly to the gephyrin G-E variant. Immunocytochemistry experiments revealed that the extent of GABAergic synaptic targeting was significantly reduced in cultured hippocampal neurons overexpressing gephyrin ΔC_4 compared with those overexpressing gephyrin WT (Fig. 5 *H* and *I*). Furthermore, overexpression of gephyrin ΔC_4 significantly decreased the density of GABAergic synapses (Fig. 5 *J* and *K*) and the frequency (but not amplitude) of mIPSCs (Fig. 5 *L*–*N*), compared with gephyrin WT. Thus, the positive charges on the C domain are crucial not only for gephyrin phase separation but also for gephyrin-mediated maintenance of GABAergic synapses.

iPSD Components Modulate Gephyrin Phase Behaviors. Gephyrin is a central scaffold at the iPSDs, anchoring diverse postsynaptic proteins such as neurotransmitter receptors, adhesion molecules, and signaling enzymes (27, 37). These proteins appear to form a network of intermolecular interactions (30), as often observed in intracellular condensates (10, 16). We thus sought to study how other proteins found in iPSDs influence the phase behaviors of gephyrin. To this end, we tested three postsynaptic proteins: GlyR, $GABA_AR$, and IQSEC3 (27, 49, 50) (Fig. 6*A*). Both GlyR and $GABA_AR$ are neurotransmitter receptors exclusively expressed at inhibitory synapses that directly interact with the gephyrin E domain through their cytoplasmic loops (51–54). Notably, the loop-binding site on the E domain is located away from a dimerizing interface between E domains (54), indicating that loop binding occurs at the spacer region of the gephyrin scaffold. To maintain in our experiments the dimeric stoichiometry of gephyrin-binding subunits found in native pentameric receptors, we fused the cytoplasmic loops of receptors to the GCN4 coiled-coil domain. A series of recent studies demonstrated that IQSEC3, a guanine nucleotide exchange factor for ADP ribosylation factor that binds to the gephyrin G domain (49, 55), is a key component that organizes GABAergic synapse density and transmission in various hippocampal circuits (56, 57).

To investigate the collective phase behaviors of these postsynaptic proteins, we coexpressed them as clients together with EGFP-gephyrin in HEK293T cells. We found that all three tested client proteins showed colocalization patterns that were seemingly similar to those of gephyrin condensates (Fig. 6 *B* and *C* and *SI Appendix*, Fig. S6*A*). To better visualize client-mediated phase modulation, we measured the concentrations of gephyrin and clients in the two coexisting phases (dilute and dense-condensate phase) in the form of ternary phase diagrams (Fig. 6*D*). The protein concentrations obtained in this manner constitute a boundary of the coexistence region within which the ternary system undergoes phase separation (58, 59). Since the shape of ternary phase

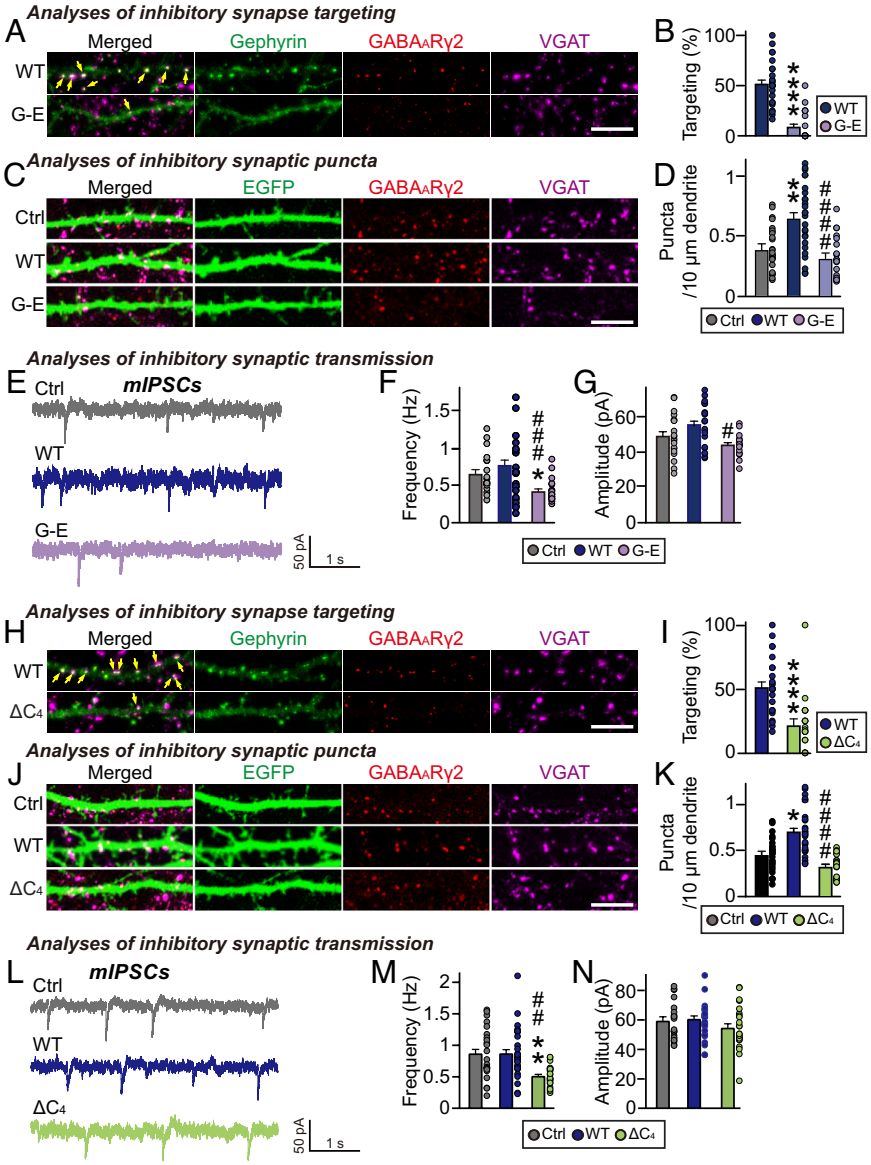

Fig. 5. The importance of the C domain in inhibitory synapse formation. (*A*) Triple-immunofluorescence images of anti-GABA$_A$Rγ2 (red), anti-VGAT (magenta) and anti-EGFP (green) antibodies in cultured hippocampal neurons transfected with EGFP-tagged gephyrin WT and G-E variant. Yellow arrows mark colocalization of gephyrin with both GABA$_A$Rγ2 and VGAT puncta. (Scale bar, 10 µm.) (*B*) Quantification of inhibitory synaptic targeting of gephyrin variants in cultured hippocampal neurons (2–3 dendrites per transfected neuron were analyzed and group-averaged). (WT and G-E $^{****}P < 0.0001$). Error bars ± SEM. (*C*) Triple-immunofluorescence images of anti-GABA$_A$Rγ2 (red), anti-VGAT (magenta) and anti-EGFP (green) antibodies in cultured hippocampal neurons transfected with EGFP alone or co-transfected with EGFP and EGFP-tagged gephyrin variants. (Scale bar, 10 µm.) (*D*) Effects of overexpression of gephyrin WT or the indicated variants on GABA$_A$Rγ2$^+$VGAT$^+$ puncta density (2–3 dendrites per transfected neuron were analyzed and group averaged). (Ctrl and WT $^{**}P = 0.0017$, WT and G-E $^{\#\#\#\#}P < 0.0001$). Error bars ± SEM. (*E–G*) Representative traces and quantification of frequency and amplitude of mIPSCs recorded from hippocampal cultured neurons transfected with the indicated gephyrin variants. (*F*) Ctrl and G-E $^{*}P = 0.0258$, WT and G-E $^{\#\#\#}P = 0.0004$; (*G*) WT and G-E $^{\#}P = 0.0351$). Error bars ± SEM; Control, n = 19; WT, n = 21; G-E, n = 19. (*H*) Triple-immunofluorescence images of anti-GABA$_A$Rγ2 (red), anti-VGAT (magenta) and anti-EGFP (green) antibodies in cultured hippocampal neurons transfected with EGFP-tagged gephyrin WT and ΔC4 variant. Yellow arrows mark colocalization of gephyrin with both GABA$_A$Rγ2 and VGAT puncta. (Scale bar, 10 µm.) (*I*) Inhibitory synaptic targeting of gephyrin variants in cultured hippocampal neurons (2–3 dendrites per transfected neuron were analyzed and group-averaged). (WT and ΔC4 $^{****}P < 0.0001$). Error bars ± SEM. (*J*) Triple-immunofluorescence images of anti-GABA$_A$Rγ2 (red), anti-VGAT (magenta) and anti-EGFP (green) antibodies in cultured hippocampal neurons transfected with EGFP alone or co-transfected with EGFP and EGFP-tagged gephyrin variants. (Scale bar, 10 µm.) (*K*) Effects of overexpression of gephyrin WT or the indicated variants on GABA$_A$Rγ2$^+$VGAT$^+$ puncta density (2–3 dendrites per transfected neuron were analyzed and group averaged). (Ctrl and WT $^{*}P = 0.0365$, WT and ΔC4 $^{\#\#\#\#}P < 0.0001$). Error bars ± SEM. (*L–N*) Representative traces and quantification of frequency and amplitude of mIPSCs recorded from hippocampal cultured neurons transfected with the indicated gephyrin variants. [(*M*) Ctrl and ΔC4 $^{**}P = 0.0031$, WT and ΔC4 $^{\#\#}P = 0.0015$]. Error bars ± SEM; Control, n = 23; WT, n = 28; ΔC4, n = 22.

diagrams is highly dependent on the type and strength of intermolecular interactions between components (59–61), characterizing the phase diagram can provide critical insights into the thermodynamic origin of the phase-separating system.

The resulting ternary phase diagrams revealed differential modulatory effects of postsynaptic proteins on the phase behaviors of gephyrin scaffolds (Fig. 6 *D* and *E*). First, we found that the saturation concentration of gephyrin was lowered by the presence of inhibitory postsynaptic receptors, an effect that was strongly observed for GlyR and less robustly for GABA$_A$R. In contrast, IQSEC3 tended to destabilize gephyrin phase separation, as evidenced by an increase in the saturation concentration. Notably, these observations are consistent with the stickers-and-spacers framework, in which binding of divalent clients to the spacer region of scaffolds can thermodynamically promote scaffold phase separation by providing extra intermolecular connectivity between scaffolds (11, 16). In line with this view, the binding affinity of GlyR for gephyrin is higher than that of GABA$_A$R (54). We also observed similar receptor-mediated gephyrin phase modulation for the gephyrin variant without the C$_4$ subregion (*SI Appendix*, Fig. S6 *B–D*), suggesting that this effect is independent of gephyrin C$_4$-based enhancement of phase separation (Fig. 3*B*). In addition to the changes in saturation concentration, we found that the degree of client partitioning also strongly depended on the client proteins: GlyR was most strongly concentrated within gephyrin condensates, whereas IQSEC3 was still enriched in condensates, albeit to a much lesser extent compared with GlyR and GABA$_A$R (Fig. 6*E*).

To gain further insight into the phase-modulatory effects of postsynaptic clients, we employed the polyphasic linkage formalism (11), which incorporates the effect of preferential binding in a ternary phase diagram such that clients have different binding affinities for scaffold molecules in dilute and dense phases. For the sake of theoretical simplicity, we assumed first-order binding polynomials, which results in a saturation concentration of scaffolds upon client addition, c_{sat}, as

$$c_{sat} = c^{o}_{sat}\frac{1 + K_A[L]}{1 + K_B[L]},$$

where c^{o}_{sat} is the saturation concentration of scaffold in the client-free condition, [L] is the client concentration, and K_A and K_B are the association constants of clients for the scaffold in dilute and dense phases, respectively. Combining this relationship with the law of mass action and lever rule (Fig. 6*F*), we obtained a system of equations that are numerically solvable (*Materials and Methods*). Using a single assumed value for c^{o}_{sat}, we constructed

ternary phase diagrams with different combinations of K_A and K_B (Fig. 6*G* and *SI Appendix*, Fig. S6*E*). As expected, the presence of clients modulated scaffold phase separation in a manner dependent on the relative binding affinities in each phase. Preferential binding toward the dense phase (high K_B/K_A ratio) led to an expansion of two-phase regime, lowering the saturation concentration of scaffolds (Fig. 6*G*). This behavior is accompanied by stronger client partitioning into condensates. We note that the ratio between association constants, rather than absolute values of them, is crucial for determining the overall shape of the ternary phase diagram (*SI Appendix*, Fig. S6*E*). Predicted phase diagrams based on the polyphasic linkage model were largely in good agreement with experimental data (Fig. 6 *D*–*G*), suggesting that differential bindings of clients to scaffolds in each phase are key

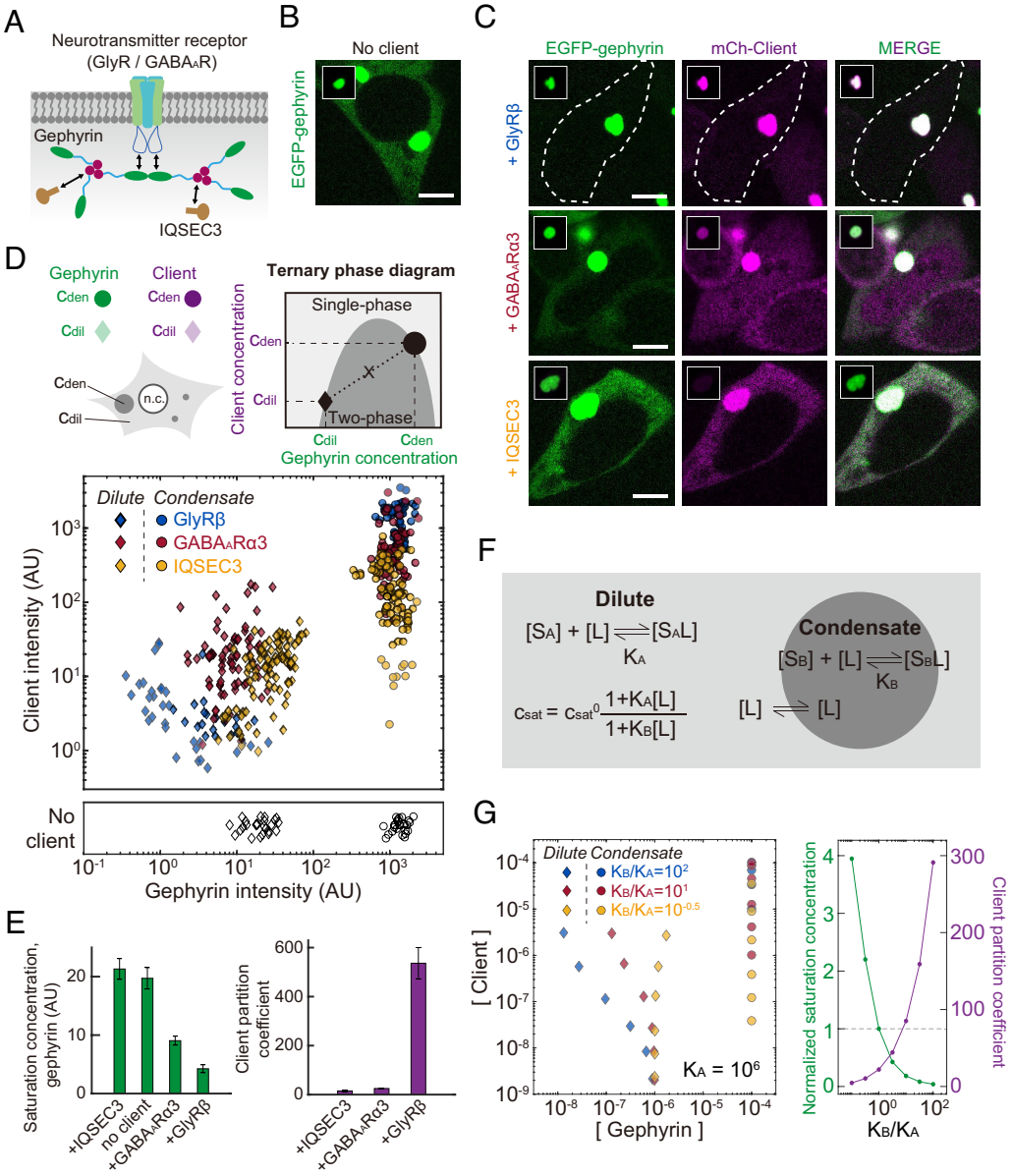

Fig. 6. iPSD components thermodynamically modulate gephyrin phase separation. (*A*) Schematic diagram of iPSD components used in this study and intermolecular interactions between them. (*B* and *C*) Fluorescence images of HEK293T cells expressing EGFP-tagged gephyrin WT alone (*B*) or coexpressing EGFP-tagged gephyrin and mCh-tagged iPSD components (*C*). Gephyrin and iPSD component expression levels are similar across these cells. For comparison, images are shown at the same brightness level. White dotted lines indicate cell boundary. Insets display gephyrin condensates in individual cells. Note that different brightness levels are used between the whole-cell images and insets. (Scale bars, 6 μm.) (*D*) (*Top*) Schematic diagram of the ternary phase diagram for gephyrin and iPSD components. Fluorescence intensities of molecules inside and outside of condensates constitute right- and left-hand boundaries of the two-phase region, respectively. (*Bottom*) Experimentally measured ternary phase diagram of gephyrin and individual iPSD components. The concentrations of the dilute- and dense phase were measured for cells containing gephyrin condensates. Data acquired with gephyrin alone are shown for comparison. Imaging conditions used in this analysis are different from those in the characterization of saturation concentrations of various gephyrin variants shown in Figs. 1–3. GlyR-β, n = 52; $GABA_AR$-α3, n = 73; IQSEC3, n = 88; no client, n = 25. (*E*) Saturation concentration of gephyrin in the presence or absence of specific iPSD components (*Left*). Partition coefficients of iPSD components, defined as a ratio of the concentration inside gephyrin condensates versus the surrounding cytoplasm (*Right*). Cells with similar expression levels are used in these quantifications. Error bars ± SEM; GlyR-β, n = 37; $GABA_AR$-α3, n = 42; IQSEC3, n = 27; gephyrin alone, n = 17. (*F*) Schematic diagram of the polyphasic linkage model. Preferential binding of clients to scaffolds in one phase over the other leads to a change in scaffold saturation concentration (*SI Appendix*). In each phase, clients exhibit equilibrium binding to scaffolds, characterized by an association constant K_i. (*G*) (*Left*) Predicted ternary phase diagrams based on the polyphasic linkage model ($K_A = 10^6\ M^{-1}$). To generate the diagrams, six different pairs of total gephyrin/client concentrations are used for each condition (*Materials and Methods*). All concentrations are in molarity. (*Right*) Changes of normalized saturation concentration and client partition coefficient by preferential binding effects. Results are obtained from model calculation using the identical total concentrations of scaffolds and clients.

determinants of observed ternary phase behaviors. Within inhibitory synapses, additional factors such as other macromolecular components and changes in protein conformation may further contribute to gephyrin phase behaviors. Collectively, our results highlight that postsynaptic components can thermodynamically modulate the phase separation of gephyrin scaffolds.

Local Accumulation of Neuroligin-2 (NLGN2) Promotes the Nucleation of Gephyrin Condensates. We then examined how gephyrin condensation can be spatiotemporally regulated by scaffold–client interactions within cells. The spatial distribution of phase-separated droplets within cells is influenced by multiple factors, including the presence of preferential nucleation sites and the degree of supersaturation (62). Thus, for proper synapse formation, gephyrin condensation must be tightly regulated in neurons. NLGN2, a postsynaptic adhesion protein exclusively expressed at GABAergic inhibitory synapses (27, 37, 50) (Fig. 7*A*), directly binds to gephyrin and plays a central role in organizing iPSDs (63). In addition, transsynaptic intermolecular interactions between NLGN2 and presynaptic neurexins are thought to be essential for proper organization of postsynaptic complexes (64).

To explore the possibility of controlling the localization of gephyrin condensates at the nucleation stage, we examined whether local accumulation of NLGN2 triggers gephyrin condensation, using the optoDroplet system to dynamically concentrate NLGN2 (Fig. 7*A*). The C-terminal intracellular domain of NLGN2, which mediates gephyrin-binding, was fused to mCh-Cry2 ($NLGN2_{cy}$-mCh-Cry2), after which its clustering behavior was tested (*SI Appendix*, Fig. S7 *A* and *B*). We found that fusing $NLGN2_{cy}$ slightly lowered the saturation concentration of optoDroplets, suggesting the presence of weak homotypic interactions between $NLGN2_{cy}$ segments. However, the phase separation–promoting effect remained marginal, resulting in a significant number of cells with no clustering. Thus, we generated an NLGN2 optoDroplet version with additional FUS IDR fusion ($NLGN2_{cy}$-FUS_N-mCh-Cry2) and demonstrated that it exhibited strong clustering capacity (*SI Appendix*, Fig. S7*B*). Using this construct, we asked whether the local accumulation of NLGN2 alters the way gephyrin undergoes phase separation. After sequential transfections of HEK293T cells with EGFP-gephyrin and $NLGN2_{cy}$-FUS_N-mCh-Cry2, we selected cells exhibiting blue light–dependent clustering of $NLGN2_{cy}$-FUS_N-mCh-Cry2 but lacking gephyrin condensates owing to low levels of expression. Strikingly, we found that gephyrin phase separation was strongly influenced by preexisting NLGN2 optoDroplets. Specifically, as gephyrin expression increased, gephyrin condensation tended to occur at the surface of NLGN2 optoDroplets (Fig. 7 *B* and *C*). Notably, gephyrin formed its own condensate phase instead of partitioning into preexisting NLGN2 optoDroplets (Fig. 7 *B*–*D*). Occasionally, the coalescence of two gephyrin condensates appears to be facilitated by intervening NLGN2 optoDroplets (Fig. 7*D*). These physical associations between gephyrin and optoDroplet condensates were completely abolished in a control construct lacking NLGN2 (Fig. 7*B*), indicating that the association between the two types of condensates is mediated by NLGN2. Thus, our findings suggest that subcellular regions in which NLGN2 highly accumulates can serve as preferential nucleation sites for gephyrin condensation.

In neurons, spatial cues in the form of local NLGN2 enrichments are provided at the cell membrane. To test whether local accumulation of NLGN2 at the membrane can still nucleate gephyrin condensates, we appended a membrane-localizing myristoylation (myr) signal to the NLGN2 optoDroplet construct (myr-mCh-Cry2-$NLGN2_{cy}$). We then expressed this construct together with EGFP-gephyrin in cultured hippocampal neurons and examined the effect of local enrichment of membrane-tethered NLGN2 on gephyrin condensates (Fig. 7*E*). Upon blue light exposure, numerous small foci enriched for the NLGN2 optoDroplet construct formed at the cell membrane (Fig. 7 *F* and *G*). Initially, the light-activated foci were highly dynamic, exhibiting frequent lateral motions (*SI Appendix*, Fig. S7 *C* and *D*), and contained no detectable gephyrin signals (Fig. 7*G*). However, as these foci subsequently grew, gephyrin accumulated at NLGN2 optoDroplets (Fig. 7*G*). A closer examination of the intensity profiles of gephyrin and NLGN2 optoDroplet construct across light-activated foci revealed that the peaks of gephyrin signals tended to be positioned toward the inside of cells, compared with NLGN2 peaks (Fig. 7*H*). These observations indicate that gephyrin is not merely recruited into membrane-tethered NLGN2 foci, but instead are consistent with nucleation of distinct gephyrin condensates at the NLGN foci, similar to results obtained in HEK293T cells. Taken together, our data demonstrate that gephyrin condensation is spatially regulated by the presence of preferential nucleation sites and likely directs the spatial organization of diverse functional complexes across inhibitory synapses.

Discussion

How the formation and localization of biomolecular condensates are regulated in cells is a central question. It is particularly relevant for condensates of which proper localization is intimately related to their cellular functions, such as in postsynaptic densities. Efficient signal transmission across neuronal synapses requires proper localization of synaptic components and their alignment between the two communicating cells. In this study, through heterologous expression in HEK293T cells, we revealed that the major iPSD scaffold, gephyrin, undergoes a concentration-dependent phase separation and the central IDR linker critically contributes to the phase behavior. We found that gephyrin condensation is thermodynamically modulated in the presence of iPSD components, with inhibitory postsynaptic receptors lowering the concentration threshold for phase separation. We further demonstrated that a spatial cue provided in the form of local accumulation of membrane-spanning adhesion protein NLGN2 can trigger gephyrin condensation in the cultured neurons, which might help organize transcellular nanodomains (65). Our data support a model in which prelocalized scaffold-interacting clients drive condensate formation by promoting nucleation of condensates as well as thermodynamically modulating scaffold phase behaviors.

The phase modulation of clients can be understood in terms of the polyphasic linkage formalism (11, 12). Recent theoretical and computational studies suggest that scaffold phase separation can be differentially influenced by clients with distinct modes of binding and valency. Monovalent clients, which bind to the sticker region of scaffolds, destabilize scaffold phase separation owing to competition with other scaffold stickers. In contrast, binding of divalent clients to spacer motifs promotes scaffold phase separation by increasing the overall stability of physical cross-links between scaffolds. In the case of gephyrin, the oligomerization interfaces of G and E domains primarily act as stickers, exhibiting homotypic association in the form of well-defined trimerization and dimerization, respectively (39, 40). Consistent with the prediction for monovalent clients targeting stickers, the coexpression of either the G or E domain with full-length gephyrin strongly suppresses gephyrin clustering (66). Viewed from this perspective, inhibitory postsynaptic receptors are divalent spacer-binding clients that can promote scaffold phase separation. Indeed, our experimental results based on artificially dimerized cytoplasmic loops fully support this modulatory role of postsynaptic receptors (Fig. 6*D*). Although we found that IQSEC3 exhibited mild suppressive

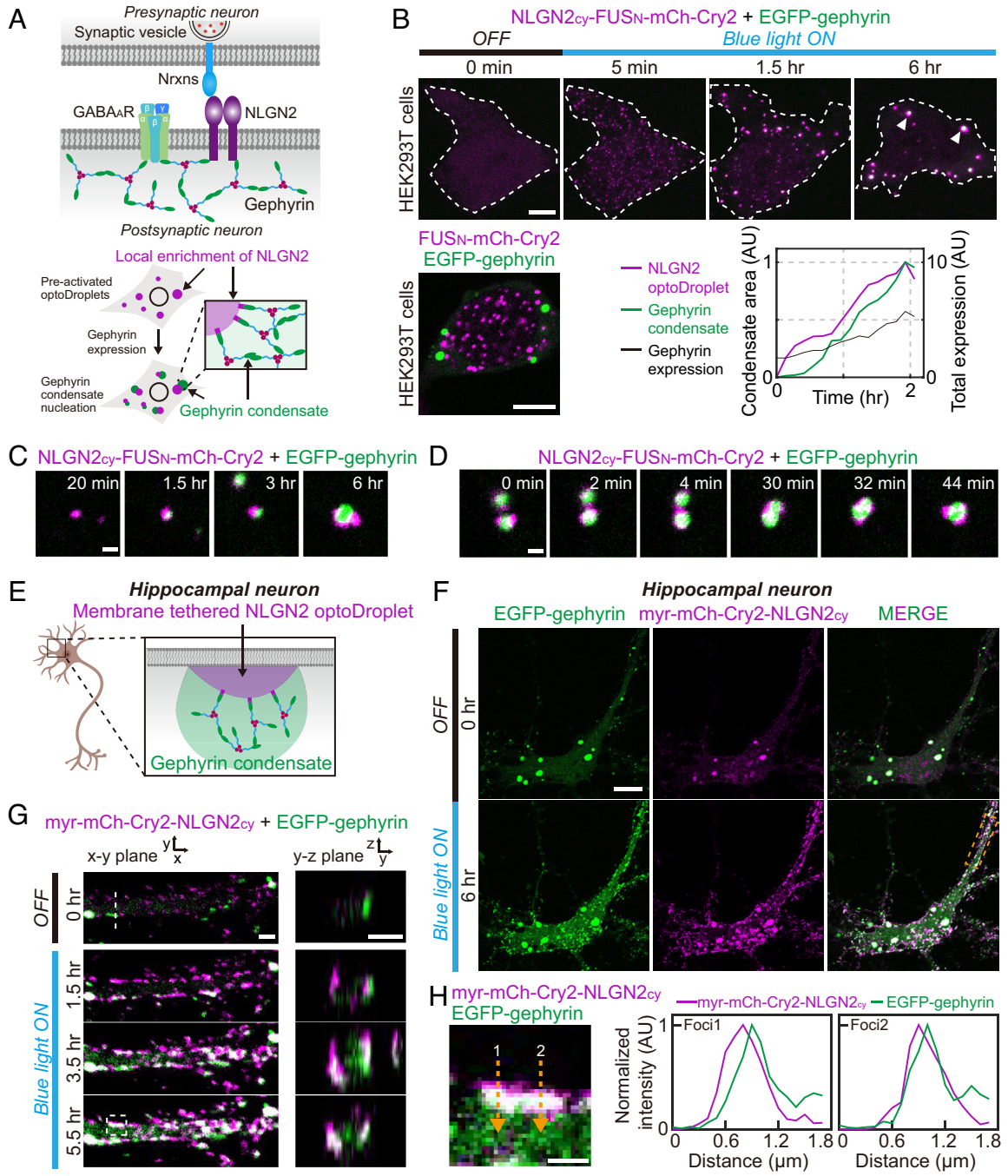

Fig. 7. Local accumulation of scaffold-binding factors triggers gephyrin condensation. (*A*) (*Top*) Schematic diagram of inhibitory synapse components. (*Bottom*) Schematic diagram of experiments probing the effect of local enrichment of NLGN2 on the nucleation of gephyrin condensates. (*B*) (*Top*) Time-lapse fluorescence images of EGFP-tagged gephyrin and NLGN2$_{cy}$-FUS$_N$-mCh-Cry2 in a HEK293T cell before and after blue-light activation. White dotted lines indicate cell boundary. White arrowheads indicate gephyrin condensates nucleated at NLGN2$_{cy}$-FUS$_N$-mCh-Cry2 clusters. Images are maximum-projected. The cell is sequentially transfected, first with the optoDroplet construct, followed 24 h after by gephyrin. After blue light–induced clustering of NLGN2$_{cy}$, an increase in gephyrin expression leads to formation of gephyrin condensates (*Bottom Right*). (Scale bar, 8 μm.) (*Bottom Left*) Fluorescence images of EGFP-tagged gephyrin and FUS$_N$-mCh-Cry2 in a HEK293T cell, 30 min after blue-light activation. (Scale bar, 6 μm.) (*C* and *D*) Zoomed-in time-lapse images of gephyrin condensation on NLGN2$_{cy}$ optoDroplet clusters (*C*) and coalescence of condensates (*D*). (Scale bar, 1 μm.) (*E*) Schematic diagram of experiments probing the effect of membrane-localized enrichment of NLGN2cy on gephyrin condensation in cultured hippocampal neurons. (*F*) Fluorescence images of EGFP-tagged gephyrin and myr-mCh-Cry2-NLGN2$_{cy}$ in a cultured mouse hippocampal neuron before and after blue-light activation. (Scale bar, 12 μm.) (*G*) Zoomed-in time-lapse images of EGFP-tagged gephyrin and myr-mCh-Cry2-NLGN2$_{cy}$ in the white dotted box in (*F*) before and after blue-light activation. Images of the cross-sections are reconstructed from z-stacks at the white dotted line. (Scale bar, 2 μm.) (*H*) Zoomed-in image of EGFP-tagged gephyrin and myr-mCh-Cry2-NLGN2$_{cy}$ in the white dashed box of figure (*G*). (Scale bar, 1 μm.) Fluorescence intensity profiles along yellow dashed arrows are shown on the *Right*.

effects on gephyrin phase separation, future studies are warranted to determine the specific IQSEC3-binding motif in the G domain and establish whether knowledge of the oligomerization state of IQSEC3 is necessary to further test the predictive power of the polyphasic linkage-based model.

Weak, multivalent interactions between self-associating IDRs often play a key role in driving phase separation (1, 35). Recently, an additional role of IDRs as phase modulators has begun to be uncovered (44, 67). In the current study, we found that the gephyrin C domain, the central IDR linker connecting G and E domains,

serves important modulatory roles in gephyrin phase separation. IDR substitution experiments showed that gephyrin phase separation driven by G/E domain-mediated oligomerization is strongly dependent on the nature of the IDR linker (Fig. 2*D*), raising the question on how the linker critically contributes to the oligomerization process. Purified gephyrin is often found as a trimeric form (39, 52), in which three long linkers, containing the E domain at the end, extend outward from the trimerized G-domain core. The contour length (i.e., fully stretched length) of the linker C domain is approximately 50 nm (*SI Appendix*, Fig. S7*E*); thus, depending on the degree of compactness of the C domain, gephyrin trimers can adopt diverse conformers of different relative sizes. Indeed, a previous study using small-angle X-ray scattering reported that purified gephyrin exhibited highly heterogenous trimer conformations, with the radius of gyration of trimeric complexes, ranging from 5 to 17 nm (68). Notably, the long flexible nature of the C domain can lead to the formation of autoinhibited gephyrin trimers, in which binding occurs between E domains within a single trimer unit (*SI Appendix*, Fig. S8). This can reduce the effective valence of the trimer to one, repressing phase separation. Alternatively, a hexamer in which two trimers are stacked on one another can be generated through a similar mechanism (69). The formation of autoinhibited trimers or hexamers may be the origin of poor clustering behaviors exhibited by purified full-length gephyrin (28, 41). In this view, gephyrin phase separation can be regulated by altering the probability of its having autoinhibitory conformers, for example, by controlling the extent of C-domain collapse (*SI Appendix*, Fig. S8). Consistent with this expectation, we indeed found that the positively charged C-domain subregion near the C-terminal end is critical for promoting gephyrin phase separation (Fig. 3). Specifically, the atomistic MC simulation revealed that the C domain adopts a highly collapsed conformation through intra- and interdomain interactions; moreover, replacing the positively charged residues with negatively charged ones reduced these interactions, leading to more expanded conformations of the C domain (Fig. 4).

Intriguingly, the gephyrin C domain harbors multiple sites for various posttranslational modifications and sites for binding to several iPSD components, including dynein light chain, Pin1, GABARAP, and tubulin (27, 37). Our findings suggest that posttranslational modifications that alter the local charge distribution can impact the network of intra- and interdomain interactions centered around the C domain, which can ultimately play a role in regulating the phase behaviors of gephyrin (30). Indeed, phosphorylation of serine residues in the C domain has been shown to affect gephyrin clustering (70, 71). In light of the polyphasic linkage model, factors that bind to the C domain can also influence gephyrin condensation. Depending on their valency and affinity, accessory factors can either promote or repress phase separation of gephyrin scaffolds through their association. It is also possible that binding of clients may tune gephyrin phase behaviors in an indirect manner by modulating the compactness of the C domain and promoting the formation of autoinhibitory complexes.

Focusing on a subset of core iPSD components, our study highlighted the fact that apart from directly controlling scaffold concentrations, scaffold phase behaviors can be regulated by scaffold-binding clients (*SI Appendix*, Fig. S8). We unequivocally demonstrated that both the spatial distribution and the expression level of clients can strongly influence the way scaffold phase separation proceeds. This client-based phase modulation is tightly linked to the sticker–spacer arrangement in scaffold architecture as well as the binding modes between scaffolds and clients. These features can collectively result in complex phase behaviors, as exhibited by intracellular condensates (72). Additionally, condensate function, such as synaptic transmission, can further contribute to the modulation of scaffold phase separation through feedback mechanisms (73, 74). Future studies will explore this interplay between condensate form and function in the context of multicomponent phase behaviors.

Materials and Methods

HEK293T (Takara, 632180) cells were cultured in DMEM (Sigma-Aldrich, D6429) supplemented with 10% fetal bovine serum (HyClone, SV30207.02) and penicillin/streptomycin antibiotics (Gibco, 15140122) at 37 °C and 5% CO_2 in a humidified incubator. HEK293T cells were transfected using Lipofectamine 3000 transfection reagent (Invitrogen, L3000015). Mouse and rat hippocampal neurons were transfected using Lipofectamine 3000 and CalPhos Kit (Clontech), respectively. A complete description of the *Materials and Methods* can be found in *SI Appendix*.

Data, Materials, and Software Availability. All study data are included in the article and/or supporting information.

ACKNOWLEDGMENTS. We thank the members of J.-M.C., J.K., and Y.S. laboratories for helpful discussions; Jinha Kim (DGIST, Korea) for technical assistance; Minsun Kim for mouse hippocampal neuron cultures; and Institute of Advanced Machines and Design at Seoul National University for administrative support. This work was supported by the National Research Foundation of Korea funded by the Korea Government (2019R1C1C1006477, RS-2023-00211612, 2022R1A5A102641311, and RS-2023-00260454 to Y.S.; 2022R1C1C2003499 to S.K.; and 2021R1C1C1010943 and 2022R1A4A1033471 to J.-M.C.), the POSCO TJ Park Foundation (POSCO Science Fellowship to J.-M.C.), the National Creative Research Initiative Program of the Ministry of Science and ICT (2022R1A3B1077206 to J.K.), and the DGIST R&D Program of the Ministry of Science and ICT (23-CoE-BT-001 to J.K.).

Author affiliations: [a]Department of Mechanical Engineering, Seoul National University, Seoul 08826, Republic of Korea; [b]Department of Brain Sciences, Daegu Gyeongbuk Institute of Science and Technology (DGIST), Daegu 42988, Republic of Korea; [c]Center for Synapse Diversity and Specificity, Daegu Gyeongbuk Institute of Science and Technology, Daegu 42988, Republic of Korea; [d]Department of Chemistry and Chemistry Institute for Functional Materials, Pusan National University, Busan 46241, Republic of Korea; [e]Department of Physics and Astronomy, Seoul National University, Seoul 08826, Republic of Korea; [f]Department of Electrical and Computer Engineering, University of Minnesota, Minneapolis, MN 55455; and [g]Interdisciplinary Program in Bioengineering, Seoul National University, Seoul 08826, Republic of Korea

Author contributions: J.-M.C., J.K., and Y.S. designed research; G.L., S.K., D.-E.H., Y.-G.E., and G.J. performed research; H.Y.P. contributed new reagents/analytic tools; G.L., S.K., D.-E.H., Y.-G.E., and G.J. analyzed data; and G.L., J.-M.C., J.K., and Y.S. wrote the paper.

1. Y. Shin, C. P. Brangwynne, Liquid phase condensation in cell physiology and disease. *Science* **357**, eaaf4382 (2017).
2. S. Alberti, A. A. Hyman, Biomolecular condensates at the nexus of cellular stress, protein aggregation disease and ageing. *Nat. Rev. Mol. Cell Biol.* **22**, 196–213 (2021).
3. S. F. Banani, H. O. Lee, A. A. Hyman, M. K. Rosen, Biomolecular condensates: Organizers of cellular biochemistry. *Nat. Rev. Mol. Cell Biol.* **18**, 285–298 (2017).
4. T. J. Nott *et al.*, Phase transition of a disordered nuage protein generates environmentally responsive membraneless organelles. *Mol. Cell* **57**, 936–947 (2015).
5. P. Li *et al.*, Phase transitions in the assembly of multivalent signalling proteins. *Nature* **483**, 336–340 (2012).
6. S. F. Banani *et al.*, Compositional control of phase-separated cellular bodies. *Cell* **166**, 651–663 (2016).
7. E. W. Martin *et al.*, Valence and patterning of aromatic residues determine the phase behavior of prion-like domains. *Science* 367, 694–699 (2020).
8. J. Wang *et al.*, A molecular grammar governing the driving forces for phase separation of prion-like RNA binding proteins. *Cell* **174**, 688–699 (2018).
9. J. A. Riback *et al.*, Composition-dependent thermodynamics of intracellular phase separation. *Nature* **581**, 209–214 (2020).
10. D. W. Sanders *et al.*, Competing protein-RNA interaction networks control multiphase intracellular organization. *Cell* **181**, 306–324 (2020).
11. K. M. Ruff, F. Dar, R. V. Pappu, Ligand effects on phase separation of multivalent macromolecules. *Proc. Natl. Acad. Sci. U.S.A.* **118**, e2017184118 (2021).
12. K. M. Ruff, F. Dar, R. V. Pappu, Polyphasic linkage and the impact of ligand binding on the regulation of biomolecular condensates. *Biophys. Rev.* **2**, 021302 (2021).

13. J. Wyman, S. J. Gill, Ligand-linked phase changes in a biological system: Applications to sickle cell hemoglobin. *Proc. Natl. Acad. Sci. U.S.A.* **77**, 5239–5242 (1980).
14. J.-M. Choi, A. S. Holehouse, R. V. Pappu, Physical principles underlying the complex biology of intracellular phase transitions. *Annu. Rev. Biophys.* **49**, 107–133 (2020).
15. J.-M. Choi, A. A. Hyman, R. V. Pappu, Generalized models for bond percolation transitions of associative polymers. *Phys. Rev. E* **102**, 042403 (2020).
16. J. R. Espinosa *et al.*, Liquid network connectivity regulates the stability and composition of biomolecular condensates with many components. *Proc. Natl. Acad. Sci. U.S.A.* **117**, 13238–13247 (2020).
17. X. Chen, X. Wu, H. Wu, M. Zhang, Phase separation at the synapse. *Nat. Neurosci.* **23**, 301–310 (2020).
18. Z. Feng, X. Chen, X. Wu, M. Zhang, Formation of biological condensates via phase separation: Characteristics, analytical methods, and physiological implications. *J. Biol. Chem.* **294**, 14823–14835 (2019).
19. X. Wu *et al.*, RIM and RIM-BP form presynaptic active-zone-like condensates via phase separation. *Mol. Cell* **73**, 971–984 (2019).
20. J. Emperador-Melero *et al.*, PKC-phosphorylation of Liprin-α3 triggers phase separation and controls presynaptic active zone structure. *Nat. Commun.* **12**, 3057 (2021).
21. D. Milovanovic, Y. Wu, X. Bian, P. De Camilli, A liquid phase of synapsin and lipid vesicles. *Science* **5671**, eaat5671 (2018).
22. D. Park *et al.*, Cooperative function of synaptophysin and synapsin in the generation of synaptic vesicle-like clusters in non-neuronal cells. *Nat. Commun.* **12**, 263 (2021).
23. N. A. Mcdonald, R. D. Fetter, K. Shen, Assembly of synaptic active zones requires phase separation of scaffold molecules. *Nature* **588**, 454–458 (2020).
24. T. Hosokawa *et al.*, CaMKII activation persistently segregates postsynaptic proteins via liquid phase separation. *Nat. Neurosci.* **24**, 777–785 (2021).
25. M. Zeng *et al.*, Reconstituted postsynaptic density as a molecular platform for understanding synapse formation and plasticity. *Cell* **174**, 1172–1187 (2018).
26. M. Zeng *et al.*, Phase transition in postsynaptic densities underlies formation of synaptic complexes and synaptic plasticity. *Cell* **166**, 1163–1175 (2016).
27. G. Choii, J. Ko, Gephyrin: A central GABAergic synapse organizer. *Exp. Mol. Med.* **47**, e158 (2015).
28. G. Bai, Y. Wang, M. Zhang, Gephyrin-mediated formation of inhibitory postsynaptic density sheet via phase separation. *Cell Res.* **31**, 312–325 (2020).
29. G. Bai, M. Zhang, Mesophasic assembly of inhibitory postsynaptic density. *Neurosci. Bull.* **37**, 141–143 (2021).
30. G. Bai, M. Zhang, Inhibitory postsynaptic density from the lens of phase separation. *Oxford Open Neurosci.* **1**, kvac003 (2022).
31. G. Meyer, J. Kirsch, H. Betz, D. Langosch, Identification of a gephyrin binding motif on the glycine receptor β subunit. *Neuron* **15**, 563–572 (1995).
32. J. Kirsch, J. Kuhse, H. Betz, Targeting of glycine receptor subunits to gephyrin-rich domains in transfected human embryonic kidney cells. *Mol. Cell. Neurosci.* **6**, 450–461 (1995).
33. Y. Shin *et al.*, Spatiotemporal control of intracellular phase transitions using light-activated optoDroplets. *Cell* **168**, 159–171 (2017).
34. A. Molliex *et al.*, Phase separation by low complexity domains promotes stress granule assembly and drives pathological fibrillization. *Cell* **163**, 123–133 (2015).
35. A. Patel *et al.*, A liquid-to-solid phase transition of the ALS protein FUS accelerated by disease mutation. *Cell* **162**, 1066–1077 (2015).
36. D. Bracha *et al.*, Mapping local and global liquid phase behavior in living cells using photo-oligomerizable seeds. *Cell* **175**, 1467–1480 (2018).
37. S. K. Tyagarajan, J. M. Fritschy, Gephyrin: A master regulator of neuronal function? *Nat. Rev. Neurosci.* **15**, 141–156 (2014).
38. F. L. Groeneweg, C. Trattnig, J. Kuhse, R. A. Nawrotzki, J. Kirsch, Gephyrin: A key regulatory protein of inhibitory synapses and beyond. *Histochem. Cell Biol.* **150**, 489–508 (2018).
39. M. Sola *et al.*, Structural basis of dynamic glycine receptor clustering by gephyrin. *EMBO J.* **23**, 2510–2519 (2004).
40. G. Schwarz, N. Schrader, R. R. Mendel, H. J. Hecht, H. Schindelin, Crystal structures of human gephyrin and plant Cnx1 G domains: Comparative analysis and functional implications. *J. Mol. Biol.* **312**, 405–418 (2001).
41. T. Saiyed *et al.*, Molecular basis of gephyrin clustering at inhibitory synapses: Role of G- and E-domain interactions. *J. Biol. Chem.* **282**, 5625–5632 (2007).
42. Y. Lin *et al.*, Formation and maturation of phase-separated liquid droplets by RNA-binding proteins. *Mol. Cell* **60**, 208–219 (2015).
43. M. T. Wei *et al.*, Nucleated transcriptional condensates amplify gene expression. *Nat. Cell Biol.* **22**, 1187–1196 (2020).
44. P. Yang *et al.*, G3BP1 is a tunable switch that triggers phase separation to assemble stress granules. *Cell* **181**, 325–345 (2020).
45. A. Vitalis, R. V. Pappu, ABSINTH: A new continuum solvation model for simulations of polypeptides in aqueous solutions. *J. Comput. Chem.* **30**, 673–699 (2008).
46. J.-M. Choi, R. V. Pappu, Improvements to the ABSINTH force field for proteins based on experimentally derived amino acid specific backbone conformational statistics. *J. Chem. Theory Comput.* **15**, 1367–1382 (2019).
47. B. Lardi-Studler *et al.*, Vertebrate-specific sequences in the gephyrin E-domain regulate cytosolic aggregation and postsynaptic clustering. *J. Cell Sci.* **120**, 1371–1382 (2007).
48. A. Bremer *et al.*, Deciphering how naturally occurring sequence features impact the phase behaviours of disordered prion-like domains. *Nat. Chem.* **14**, 196–207 (2022).
49. J. W. Um, Synaptic functions of the IQSEC family of ADP-ribosylation factor guanine nucleotide exchange factors. *Neurosci. Res.* **116**, 54–59 (2017).
50. J. Ko, G. Choii, J. W. Um, The balancing act of GABAergic synapse organizers. *Trends Mol. Med.* **21**, 256–268 (2015).
51. P. Pfeiffer, D. Graham, H. Betz, Purification by affinity chromatography of the glycine receptor of rat spinal cord. *J. Biol. Chem.* **257**, 9389–9393 (1982).
52. N. Schrader *et al.*, Biochemical characterization of the high affinity binding between the glycine receptor and gephyrin. *J. Biol. Chem.* **279**, 18733–18741 (2004).
53. Y. K. Eun *et al.*, Deciphering the structural framework of glycine receptor anchoring by gephyrin. *EMBO J.* **25**, 1385–1395 (2006).
54. H. M. Maric *et al.*, Molecular basis of the alternative recruitment of GABAA versus glycine receptors through gephyrin. *Nat. Commun.* **5**, 5767 (2014).
55. J. W. Um *et al.*, IQ motif and SEC7 domain-containing protein 3 (IQSEC3) interacts with gephyrin to promote inhibitory synapse formation. *J. Biol. Chem.* **291**, 10119–10130 (2016).
56. S. Kim *et al.*, Loss of IQSEC3 disrupts GABAergic synapse maintenance and decreases somatostatin expression in the hippocampus. *Cell Rep.* **30**, 1995–2005 (2020).
57. S. Kim *et al.*, Npas4 regulates IQSEC3 expression in hippocampal somatostatin interneurons to mediate anxiety-like behavior. *Cell Rep.* **36**, 109417 (2021).
58. G. L. Dignon, R. B. Best, J. Mittal, Biomolecular phase separation: From molecular driving forces to macroscopic properties. *Annu. Rev. Phys. Chem.* **71**, 53–75 (2020).
59. Y. Shin, Rich phase separation behavior of biomolecules. *Mol. Cells* **45**, 6–15 (2022).
60. D. Deviri, S. A. Safran, Physical theory of biological noise buffering by multicomponent phase separation. *Proc. Natl. Acad. Sci. U.S.A.* **118**, e2100099118 (2021).
61. T. Kaur *et al.*, Sequence-encoded and composition-dependent protein-RNA interactions control multiphasic condensate morphologies. *Nat. Commun.* **12**, 872 (2021).
62. Y. Shin *et al.*, Liquid nuclear condensates mechanically sense and restructure the genome. *Cell* **175**, 1481–1491 (2018).
63. A. Poulopoulos *et al.*, Neuroligin 2 drives postsynaptic assembly at perisomatic inhibitory synapses through gephyrin and collybistin. *Neuron* **63**, 628–642 (2009).
64. E. R. Graf, X. Zhang, S. X. Jin, M. W. Linhoff, A. M. Craig, Neurexins induce differentiation of GABA and glutamate postsynaptic specializations via neuroligins. *Cell* **119**, 1013–1026 (2004).
65. K. C. Crosb *et al.*, Nanoscale subsynaptic domains underlie the organization of the inhibitory synapse. *Cell Rep.* **26**, 3284–3297 (2019).
66. M. Calamai *et al.*, Gephyrin oligomerization controls GlyR mobility and synaptic clustering. *J. Neurosci.* **29**, 7639–7648 (2009).
67. J. Guillén-Boixet *et al.*, RNA-induced conformational switching and clustering of G3BP drive stress granule assembly by condensation. *Cell* **181**, 346–361 (2020).
68. B. Sander *et al.*, Structural characterization of gephyrin by AFM and SAXS reveals a mixture of compact and extended states. *Acta Crystallogr. Sect. D Biol. Crystallogr.* **69**, 2050–2060 (2013).
69. J. Herweg, G. Schwarz, Splice-specific glycine receptor binding, folding, and phosphorylation of the scaffolding protein gephyrin. *J. Biol. Chem.* **287**, 12645–12656 (2012).
70. C. E. Flores *et al.*, Activity-dependent inhibitory synapse remodeling through gephyrin phosphorylation. *Proc. Natl. Acad. Sci. U.S.A.* **112**, E65–E72 (2015).
71. S. K. Tyagarajan *et al.*, Regulation of GABAergic synapse formation and plasticity by GSK3β-dependent phosphorylation of gephyrin. *Proc. Natl. Acad. Sci. U.S.A.* **108**, 379–384 (2011).
72. T. Kim *et al.*, RNA-mediated demixing transition of low-density condensates. *Nat. Commun.* **14**, 2425 (2023).
73. J. E. Henninge *et al.*, RNA-mediated feedback control of transcriptional condensates. *Cell* **184**, 207–225 (2021).
74. B. Tsang *et al.*, Phosphoregulated FMRP phase separation models activity-dependent translation through bidirectional control of mRNA granule formation. *Proc. Natl. Acad. Sci. U.S.A.* **116**, 4218–4227 (2019).